Eur. Phys. J. B **12**, 497–508 (1999)

THE EUROPEAN PHYSICAL JOURNAL B

EDP Sciences

Structural investigation of a new variety of the low dimensional conductor $(PO_2)_4(WO_3)_{2m}$ with $2m = 5 + 5$: $P_4W_{10}O_{38}$*

P. Roussel[1,a], P. Foury-Leylekian[2], B. Domengès[1], D. Groult[1], P. Labbé[1], and J.-P. Pouget[2,3]

[1] Laboratoire CRISMAT[b], ISMRA-Université de Caen, 14050 Caen Cedex, France
[2] Laboratoire de Physique des Solides[c], Université de Paris-Sud, 91405 Orsay Cedex, France
[3] Département Sciences Physiques et Mathématiques, CNRS, 3 rue Michel-Ange, 75794 Paris Cedex 16, France

Received 12 March 1999 and received in final form 20 May 1999

Abstract. A new variety of $P_4W_{10}O_{38}$, $m = 5$ member of the monophosphate tungsten-bronze family with pentagonal tunnels ($MPTB_p$), $(PO_2)_4(WO_3)_{2m}$, has been isolated and studied by X-ray diffraction measurements. The structure has been solved by direct methods from single crystal X-ray data. The monoclinic unit cell corresponds to a regular stacking of WO_3-type slabs which are all five-WO_6-octahedra thick and connected through PO_4 tetrahedra. This structure is comparable to that previously described for the $MPTB_p$'series with $m = 4$ ($P_4W_8O_{32}$) and $m = 6$ ($P_4W_{12}O_{44}$). An X-ray diffuse scattering investigation has revealed that this member is subjected to charge density wave instabilities (CDW) located on chains running along the $\mathbf{a} \pm \mathbf{b}$ directions. Two CDW transitions have been observed at $T_{c_1} = 83\,(\pm 5)$ K and $T_{c_2} = 60\,(\pm 2)$ K, bearing some resemblance with those exhibited by the $m = 4$ member. The corresponding modulation wave vectors can be accounted for by a hidden nesting mechanism which connects the crossing points of differently oriented quasi-planar Fermi surfaces, as found for the low m (4 and 6) members of the MPTB's.

PACS. 61.10.-i X-ray diffraction and scattering – 61.14.-x Electron diffraction and scattering – 71.45.Lr Charge-density-wave systems

1 Introduction

The **M**ono**P**hosphate **T**ungsten **B**ronzes with **p**entagonal tunnels ($MPTB_p$) form a new family of low dimensional conductors with the general formula $(PO_2)_4(WO_3)_{2m}$ where m is an integer. Recently, the properties of different members were investigated on single crystals ranging from $m = 4$ to $m = 14$. Very interesting electronic behaviours were observed. In particular electron-transport measurements as well as X-ray diffuse scattering investigations have shown the formation of several successive incommensurate charge-density-wave (CDW) transitions in all the members with $m \leq 13$, as well as the onset of superconductivity in the $m = 7$ member [1,2]. In the $m = 4$ and 6 members the CDW modulation is sinusoidal [3] and it is due to a hidden nesting mechanism [4,5] involving portions of differently oriented quasi-one dimensional Fermi surfaces. For $7 \leq m \leq 13$, the CDW modulation is non-sinusoidal, a feature which could be the fingerprint of important electron-phonon and/or electron-electron interactions [6]. In addition, a commensurate transition is observed for $m \geq 9$, with a unit cell doubling, which bears some resemblance to the antiferroelectric transition exhibited by WO_3 (*i.e.* $(PO_2)_4(WO_3)_{2m}$ in the limit $m \to \infty$ [7]).

The structural packing of the different members were determined and analysed up to $m = 12$. Seven structural determinations have been published using single crystals and X-ray diffraction ($m = 2, 4, 5, 6, 7, 8$ and 12). The examination of these different crystal structures leads to the same general building rules with some local variations inducing slight distortions and symmetry changes [8–13]. All these crystal structures are indeed described by the association of quite regular WO_6 octahedra and PO_4 tetrahedra sharing corners. WO_3-type slabs are joined through PO_4 tetrahedra, forming at the junction large cages with pentagonal windows to which the subscript p refers to in the $MPTB_p$ name. Two important facts must be emphasised: first, it appears that cations of the size of Na^+ can be inserted into the cage, with a concentration $x \leq 1$ but only for $m \geq 6$ [14]; second, the successive slabs of WO_3-type are in general arranged in a chevron shape and they have all exactly the same thickness so that the symmetry found is orthorhombic or possibly monoclinic

* Structure factors are only available in the electronic version at `http://www.edpsciences.org`

[a] e-mail: `pascal.roussel@ismra.fr`
[b] CNRS UMR 6508
[c] CNRS UMR 8502

(pseudo-orthorhombic) due to slight local distortion. However, there is one exception always regarded as a curiosity in the family: $P_4W_{10}O_{38}$ ($m = 5$), whose structure is composed of ordered successive slabs, corresponding alternately to $m = 4$ and $m = 6$, building a regular intergrowth structure [10] which was never observed for any other members of the $MPTB_p$'family. The expected "regular" structure $2m = 5+5$ had never been detected, neither by X-ray nor by electronic diffraction. This result seemed quite strange, but we came to accept that the intergrowth phase ($2m = 4 + 6$) was the only stable one and that the regular one ($2m = 5 + 5$) was unfortunately and surprisingly non-existent.

Recently, a search for the best crystal growth conditions allowing single crystals of the $MPTB_p$ family to be obtained with sizes suitable for physical measurements, led us to identify the hitherto missing crystal variety of the $2m = 5 + 5$ "regular" member. The present paper deals with the room temperature crystal-structure determination and the low temperature structural instabilities of this new odd regular member of the $MPTB_p$ series, interpolating between the $m = 4$ and 6 regular members whose physical properties are well documented. Electron-transport properties of the regular $2m = 5 + 5$ member have been published elsewhere [15].

2 Experimental procedures

2.1 Crystal growth

The $m = 5$ single crystals were selected from a preparation corresponding to $P_4W_8O_{32}$ ($m = 4$ member) following a procedure that was previously reported [13]. A mixture of $(NH_4)_2HPO_4$ and WO_3 is first heated to 600 ℃ in air to decompose the ammonium phosphate. Second, an appropriate amount of metallic tungsten is added before the mixture is heated at 950 ℃ for 48 hours in a evacuated silica tube. Polycrystalline $P_4W_8O_{32}$ is thus obtained.

A chemical vapour-transport technique is then used for crystal growth. A charge of about 2 g of $P_4W_8O_{32}$ powder is packed in a quartz tube of 20 cm length and 1.8 cm internal diameter, sealed under vacuum. The tube is inserted in a horizontal furnace having two heating zones, 20 cm apart. The temperature of the furnace is progressively increased to 1 000 ℃ by successive steps of 200 ℃. For crystal growth special attention is paid to the temperature gradient which is applied along the length of the quartz tube. The conditions which were retained are 1 200 ℃ for the hot zone and 1 000 ℃ for the cold zone. The tube is kept in the furnace for one week and then slowly cooled down to 25 ℃.

Plate-like crystals grow in the central part of the tube with typical sizes of $3 \times 3 \times 0.2$ mm^3. Most of the crystals are purple coloured and correspond to $P_4W_8O_{32}$. Others are two tone blue-purple with golden edges: they were identified as the $2m = 5 + 5$ regular phase.

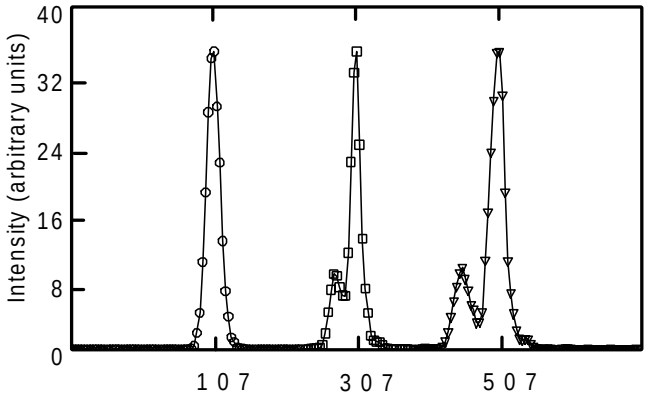

Fig. 1. X-ray profile of the $h07$ reflections ($h = 1, 3$ and 5) showing their splitting due to the twinning. Note that the splitting increases when h increases.

2.2 X-ray preliminary study

The crystals were selected from the preparation by means of a binocular microscope, choosing samples for which light reflection was neither clearly purple, as for the $m = 4$ samples, nor clearly blue as for the $m = 6$ samples. Note however that some of the selected samples turned out to be $m = 4$ which proves that the visual selection is in fact not simple and quite primitive. The selected crystals were tested with a Weissenberg camera in order to check the expected lattice parameters, the apparent orthorhombic symmetry as well as the quality of the diffraction. For most of the crystals tested, the lattice parameters are $a \approx 5.3$ Å, $b \approx 6.5$ Å, $c \approx 20.5$ Å and the three angles α, β and γ are close to 90°. These values are in agreement with those expected for the $m = 5$ regular member of the $MPTB_p$ family and different from those of the "intergrowth" ($2m = 4 + 6$) phase which exhibits a β angle of nearly 96°. Thus these two varieties can be easily distinguished by inspection of a zero level $[h0l]$ Weissenberg pattern.

However, for all the crystals investigated, we observed on the Weissenberg patterns a systematic splitting of the spots, increasing with increasing h indices. On the contrary, the $[00l]$ spots observed on the zero level pattern and the $[01l], [02l], \ldots$ spots observed on the upper level patterns are not split. Analogous features were observed for the odd $m = 7$ member of the series [12]. According to this previous structural study, two conclusions can be drawn: first, the actual symmetry of the $2m = 5+5$ regular member is pseudo-orthorhombic; and second, the crystals are systematically twinned.

2.3 CAD4 goniometer investigation

To establish the twin law, a crystal plate bounded by {100}, {010} and {001} faces was mounted on the goniometer head of a Enraf-Nonius CAD4 diffractometer. A first cell determination confirmed that the β value was not strictly 90°, proving the slight monoclinic distortion of the cell. To determine the twin element, systematic scans of h, k, l reflections (k being fixed) were collected along

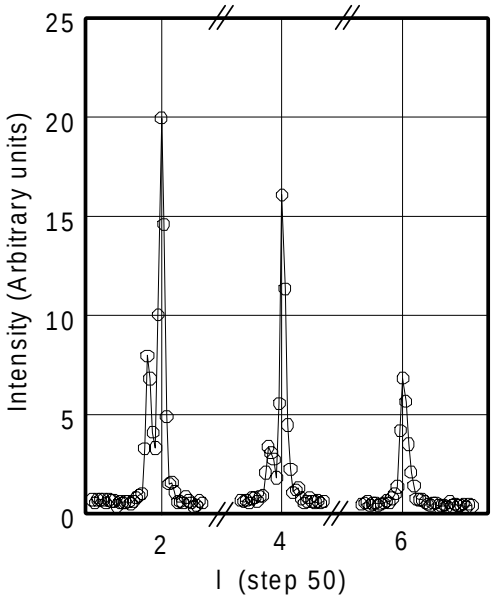

Fig. 2. X-ray profile of the $40l$ reflections ($l = 2, 4$ and 6). Note that the 406 reflection is a single one. Such reflections have been used to refine accurately the unit cell parameters.

rows parallel to $\mathbf{a}^*$ by increasing l, or parallel to $\mathbf{c}^*$, by increasing h. In this last type of scan, one observes that the separation of the diffraction peaks, due to the two components of the twin, increases proportionally to the h value (Fig. 1). This observation is consistent with two monoclinic lattices related by a twin element which can be, for instance in the reciprocal space, a plane normal to $\mathbf{c}^*$. Thus, the indices h', k', l' of a reflection located near the reflection h, k, l are obtained through the matrix relationship:

$$(h'k'l') = (hkl)\begin{pmatrix} 1 & 0 & 0 \\ 0 & 1 & 0 \\ 0 & 0 & \overline{1} \end{pmatrix}.$$

The related elements, in real space, are then the $(\mathbf{a}, \mathbf{b})$ plane itself which is parallel to the WO_3-type slabs.

The next step was to refine the cell parameters by taking the twins into account. Indeed, only the reflections with $h = 0$ have a reciprocal space position unaffected by the twin, while the splitting of the reflections with $h \neq 0$ induces a shift of the centre of gravity of the reflection and therefore leads to approximate values for the cell parameters. To solve this problem and to obtain the best orientation of the crystal, systematic scans along rows parallel to $\mathbf{c}^*$ were recorded and analysed. Sometimes, one observes only one of the two expected components because one of the structure factors $F(hkl)$ or $F(h'k'l')$ can be zero or close to zero, as seen in Figure 2 for the [406] reflection. Sixteen reflections of this type, with $h > 0$, were indexed and refined leading to the cell parameters listed in Table 1.

The last step before data-collection, was to adjust the data parameters as well as the best scan-type, scan angles and counter aperture. To solve correctly the structure it is necessary to take the twin into account. This is possible with the refinement program used, JANA98 [16], if the intensity of the two sets of Bragg reflections can be collected either together or separately. In our crystal, β being close to 90°, the two sets are always close to each other and sometimes superimposed. It is therefore necessary to check the data-collection parameters to be sure that the measurement adds correctly the intensities of the two components, in order to use the relation:

$$F^2(H) = \nu_1 F^2(HT_1) + \nu_2 F^2(HT_2)$$

where ν_i is the volume fraction of the ith component and T_i the matrix relating the reciprocal wave vectors of the two twins; in our case, T_1 is the identity matrix and T_2 the matrix written above.

In addition, each Bragg reflection is split into two components owing to the presence of the incoming $K\alpha_1$ and $K\alpha_2$ incident X-ray radiation. Thus, the relative distribution of the peak intensities seen in the $\Omega - \theta$ plane are such as shown Figure 3, where the doublet $K\alpha_1$ and $K\alpha_2$ for the two components of the twin of a $[h00]$ reflection is visualised. It clearly appears that the choice of the scan direction can favour either the collection of the $K\alpha_1$ reflection of the two twin components (for example pure Ω-scan; type = 0, since the θ angles are the same)

Table 1. Crystal data and details of the structure determination.

Crystal data	
Empirical formula	$P_4W_{10}O_{38}$
Formula weight	2 570.4
Crystal system	Monoclinic
Space group	$P2_1/n$ (Nr. 14)
a, b, c [Å]	5.283 1(6) 6.567 4(9) 20.451(5)
α, β, γ [°]	90 90.40(1) 90
V [Å^3]	709.6(2)
Z	1
D_{calc} [g/cm^3]	6.015
$F(000)$	1 104
μ (Mo Kα) [cm^{-1}]	407.1
Crystal size [mm]	$0.10 \times 0.06 \times 0.005$
Data collection	
Temperature [K]	293
Radiation [Å]	Mo K$_\alpha$ 0.710 73
Theta min-max [°]	3.3, 45.0
Scan (type and range) [°]	0 $1.60 + 0.35 \tan\theta$
Hor. and vert. aperture [mm]	1.60 1.00
Standard reflections	3
Dataset	$-10:10$; $0:13$; $-40:40$
Tot., uniq. data, R_{int}	11 659, 5 834, 0.041
Observed data [$I > 3.0\sigma(I)$]	1 886
Refinement	
Number of reflections used, number of parameters	891 67
R, wR, S	0.028 2, 0.025 4, 1.74
Weighting scheme	$w = 1/\sigma^2$
Max. and av. shift/error	0.000 2, 0.000 0
Twin ratio	0.22(1)

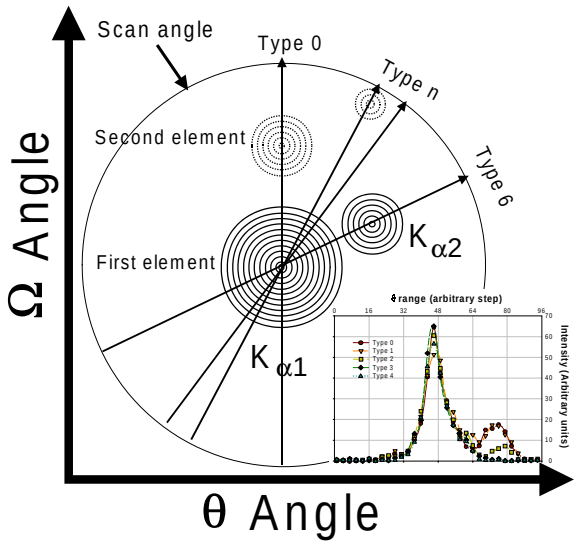

Fig. 3. Schematic plot showing the distribution of the peak intensities in the Ω–θ plane for a $h00$ reflection. The type of scan is defined by $\Omega - \frac{n\theta}{3}$; so a type 0 scan is a pure Ω scan and a type 6 scan a Ω–2θ one. Insert: experimental X-ray profile of the $50\overline{7}$ reflection along various type n scans, showing for the type 0 scan the two twin components.

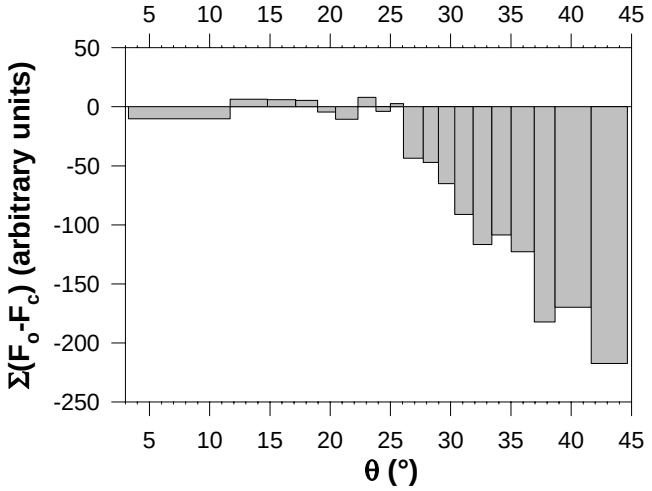

Fig. 4. Diagram $\sum(F_o - F_c)$ *versus* θ showing that for $\theta \geq 26°$, the calculated structure factor F_c is systematically overestimated. This is due to the type of scan which, for high θ, does not take into account the $K_{\alpha 2}$ contribution of the incident X-ray beam (see Fig. 3).

or the global collection of the $K\alpha$ doublet of only one of the twin components (for example Ω–2θ scan; type = 6). In a more general case one can use an intermediate type of scan, but, as the θ angle of the two $K\alpha_1$ reflections remains close to each other, the addition of the intensities is rather performed for a pure Ω-scan (type = 0). This has been checked for several reflections, as illustrated in the lower-right insert of Figure 3 for the $[50\overline{7}]$ reflection. However, it is obvious that these measurements are only valid for small values of θ such that the separation of the doublet $K\alpha_1$ and $K\alpha_2$ remains small. For greater values of θ, the intensity measurements are systematically affected by the separation of the reflections. This was the case for θ greater than 26° as shown below.

2.4 Data collection and structure determination

The data collection was performed using the experimental parameters given in Table 1. The background was measured extending the scan angle on each side of a Bragg reflection. At regular intervals, the intensity of three Bragg reflections were measured in order to verify both the stability of the crystal and the standing of the experimental device. A total of 11 659 reflections was recorded for two equivalent monoclinic areas. The intensities were corrected for the Lorentz and polarisation effects as well as for absorption using a method based on the precise morphology of the crystal. This method leads to a decrease of the $R_{\rm int}$ value from 9.9% to 4.1%.

The structure determination was performed using a set of 1 886 independent reflections with $I > 3\sigma(I)$. A preliminary structural model was found by direct methods using the SIR97 [17] program. Starting from the location of the cations, all the oxygen positions were found by difference series. Then, all the atomic coordinates were refined by least squares including the twin rate $(V_2/(V_1 + V_2))$ using the JANA98 program [16]. As can be seen in Figure 4, which shows a statistical analysis of the results ($F_O - F_C$ with respect to θ), the calculated structure factors are systematically greater than the observed ones for $\theta \geq 26°$. As a consequence, the final refinement was performed using 891 reflections with $\theta < 26°$. Table 2 gives the atomic coordinates deduced from such a refinement. Selected interatomic distances are also given in Table 3.

2.5 Electron microscope study

In order to characterize the $m = 5$ crystals at a microscopic scale, samples were chosen from the same batch as the single crystal studied by X-ray diffraction. They were gently crushed in an agate mortar in n-butanol and deposited on a holey carbon coated copper grid. An overall characterization of the batch could then be performed, as well as a nanoscale study. Fragments of several micro-crystals were investigated in this way. The electron diffraction (E.D.) study was performed with a JEM200CX equipped with a tilting rotating goniometer (±60°), which allows the reciprocal space reconstruction. The high-resolution electron-microscope (HREM) study was performed with a TOPCON 2B electron microscope equipped with a ±10° double tilt goniometer and an objective lens with a spherical aberration constant of 0.4 mm. Experimental images were scanned using a 600 dpi resolution scanner. High resolution image calculations were performed using the multislice method of the EMS package.

Table 2. Final coordinates and anisotropic displacement parameters.

Atom	x	y	z	U [Å^2]
W1	1/2	1/2	1/2	0.006 8(2)[a]
W2	−0.003 1(2)	0.172 62(8)	0.426 37(2)	0.006 6(1)[a]
W3	−0.502 1(2)	−0.161 53(7)	0.353 41(2)	0.005 9(1)[a]
P	−0.012 0(9)	−0.470 0(4)	0.303 0(1)	0.003 2(6)
O1	−0.277(2)	0.318(2)	0.456 1(5)	0.010(2)
O2	0.778(2)	0.649(2)	0.535 3(6)	0.019(3)
O3	−0.501(2)	−0.326 0(10)	0.425 9(4)	0.014(2)
O4	0	0	1/2	0.011(2)
O5	0.006(3)	0.340 0(10)	0.344 9(4)	0.018(2)
O6	−0.233(2)	−0.014(2)	0.380 3(5)	0.018(3)
O7	−0.726(2)	0.016(2)	0.387 8(5)	0.009(2)
O8	−0.513(2)	−0.025(1)	0.267 6(4)	0.017(2)
O9	−0.268(2)	−0.363(2)	0.310 9(5)	0.019(3)
O10	0.201(2)	−0.330(2)	0.321 1(5)	0.026(3)

[a] atoms refined anisotropically: $U_{\text{eq}} = \frac{1}{3}\sum_{i=1}^{3}\sum_{j=1}^{3} U^{ij} a_i^* a_j^* \mathbf{a}_i \mathbf{a}_j$.

Atom	U^{11}	U^{22}	U^{33}	U^{23}	U^{13}	U^{12}
W1	0.008 8(3)	0.004 4(3)	0.007 3(3)	0.000 6(3)	0.004 7(5)	0.000 4(5)
W2	0.008 2(2)	0.003 8(2)	0.007 7(3)	0.000 3(2)	0.003 5(4)	−0.000 2(3)
W3	0.007 5(2)	0.003 1(2)	0.007 2(3)	0.000 4(2)	0.004 5(4)	0.000 3(4)

Table 3. Selected interatomic distances (Å).

	W1	W2	W3	P
O1	1.91(1) × 2	1.84(1)		
O2	1.90(1) × 2	1.84(1)		
O3	1.898(8) × 2		1.834(8)	
O4		1.885(5)		
O5		1.997(8)		1.516(8)
O6		1.96(1)	1.80(1)	
O7		1.96(1)	1.81(1)	
O8			1.971(8)	1.495(8)
O9			2.01(1)	1.53(1)
O10			2.03(1)	1.50(1)

2.6 X-ray diffuse scattering experiments

The X-ray diffuse scattering study was performed using the $\lambda_{\text{Cu}} = 1.542$ Å radiation from either a classical tube or a rotating anode (for intensity measurements) equipped with a doubly bent graphite monochromator. The investigation was performed with the so called fixed film-fixed crystal method, well adapted to detect weak diffuse scattering. The intensity of selected reflections was then measured with an Ar-methane gas linear detector. The diffraction set up was equipped with a cryocooler operating from room temperature down to 25 K. The sample studied was a thin single crystal (4–5 mm^2 by 0.1 mm) in order to reduce the X-ray absorption.

3 Results

3.1 Electron diffraction and HREM investigations

The first aim of the electron-diffraction study was to verify the homogeneity of the batch, in order to evaluate the amount of $2m = 5 + 5$ $MPTB_p$ crystals. Electron diffraction allows a rather easy distinction between the pseudo-orthorhombic (*i.e.* $2m = 5 + 5$ structure) and the monoclinic ($2m = 4 + 6$ structure) forms of $m = 5$ $MPTB_p$, not only through reciprocal reconstruction but also through a careful analysis of the $[0kl]$ and $[hhl]$ patterns. Indeed, whereas the monoclinic deformation of the $2m = 4 + 6$ structure is difficult to measure through direct observation on the microscope, the loss of the mirror perpendicular to the $\mathbf{c}^*$ axis is clearly seen in the intensity differences of the (hkl) and $(hk\bar{l})$ reflections, especially those of the perovskite subcell. To see this, consider for example the building principle of the $MPTB_p$ structure with $m = 4$. The structure is based on perovskite-like blocks made of corner sharing WO_6 octahedra joined through PO_4 tetrahedra located in the $(112)_p$ (sub-p for perovskite) plane (Fig. 5a). These blocks are infinite along the $[1\bar{1}0]_p$ direction. The structure is then built up by a rotation-like procedure *i.e.* a π rotation of one block out of two about the $[11\bar{1}]_p$ axis as shown Figure 5b. Pentagonal-like tunnels are formed at the junction of successive slabs, as shown Figure 5c. Except for the $2m = 4 + 6$ monoclinic form, every slab contains the same number of octahedra corresponding to the formula $-(PO_2)-(WO_3)_m-(PO_2)-(WO_3)_m-$. Indeed along the $[100]_p$ or the $[010]_p$ directions, as can be seen in the $[1\bar{1}0]_p$ projection, one observes segments of m WO_6 octahedra ending with two PO_4 tetrahedra.

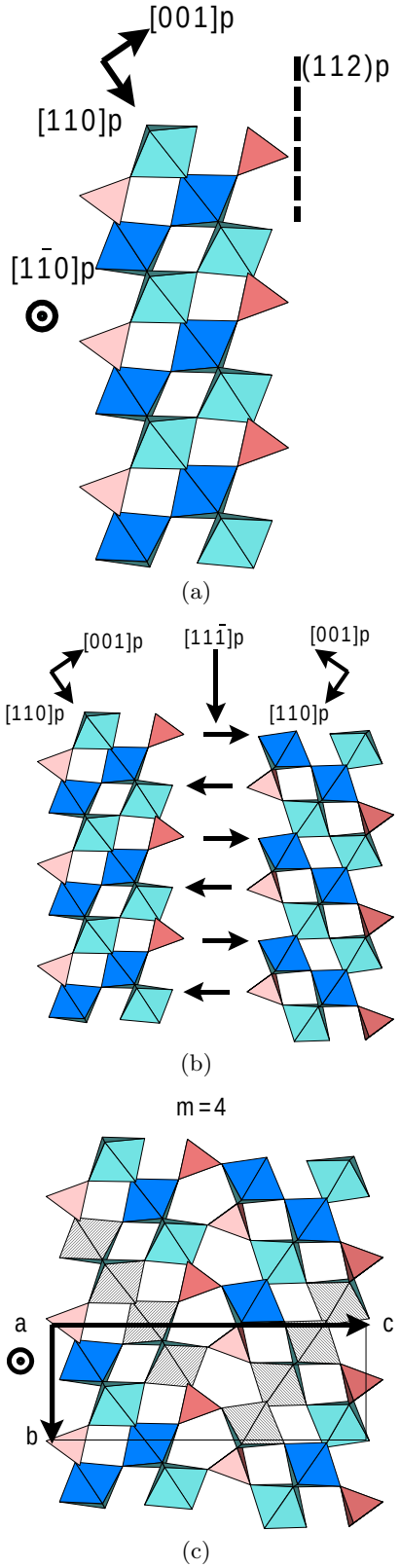

Fig. 5. Representation of the building principle of the $MPTB_p$ structure and its geometric relationships with the perovskite substructure. (a) Isolated mixed block of formulation $-(PO_2)-(WO_3)_4-(PO_2)-$; (b) twin-like procedure of construction of two successive layers; (c) resulting $MPTB_p$ structure.

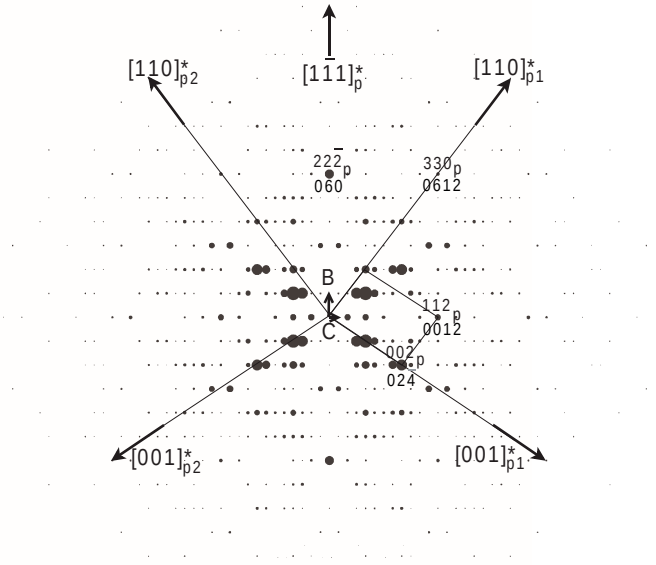

Fig. 6. Calculated [100] electron-diffraction pattern with the indexation of stronger dots both in the perovskite subcell (suffix p) and the $m = 4$ $MPTB_p$ cell. The two perovskite reciprocal spaces, related by the twin symmetry shown Figure 5b, are denoted by the suffixes p1 and p2.

The geometric relationships between the $MPTB_p$ lattice parameters and the perovskite row directions are the following: $\mathbf{a} \parallel [1\bar{1}0]_p$, $\mathbf{b} \parallel [11\bar{1}]_p$ and $\mathbf{c} \parallel [112]_p$, so that the usual direction of projection of the structure, *i.e* [100], corresponds to $[1\bar{1}0]_p$. Also, one has the following relationships: $(100) \parallel (1\bar{1}0)_p$, $(010) \parallel (11\bar{1})_p$ and $(001) \parallel (112)_p$. In consequence, electron-diffraction patterns show strong spots which correspond to the perovskite subcell and which can thus be easily indexed. Figure 6 shows the [100] electron-diffraction pattern of the $m = 4$ member with stronger spots indexed in the $MPTB_p$ cell as well as in the perovskite subcell. Along the reciprocal $\mathbf{c}^*$ axis the strongest spot is observed for $l = 12$, *i.e.* $[2 \times (m + 2)]$th; the "thickness", $\mathbf{c}/2$, of a block including m octahedra and two tetrahedra being close to $m + 2$ times d_{112p}. This feature is verified for each member of the family; furthermore, the higher the value of m, the higher is the number of octahedra (*i.e.* perovskite elemental units) in a slab, and the stronger is the intensity of the subcell reflections (see Tab. 6). The rotation-like procedure that builds the $MPTB_p$ structure is also well imaged on the [100] E.D. pattern (Fig. 6) where two sets of stronger dots, symmetrical with respect to the $\mathbf{b}^*$ (or the $[hh-h]_p$) reciprocal direction are observed.

These features are well imaged on the [100] E.D. patterns of both forms of $m = 5$ members. The E.D. patterns of the pseudo-orthorhombic form $2m = 5 + 5$, show spots with a symmetrical appearance due to the rotated-like subcell sets (Fig. 7a) whereas those of the monoclinic form $2m = 4+6$, resulting from the intergrowth of 4 and 6 octahedra wide perovskite-type slabs, show a disymmetric aspect of the rotated-like subsets (Fig. 7b) (the spots corresponding to the $m = 4$ part being of lower intensity than

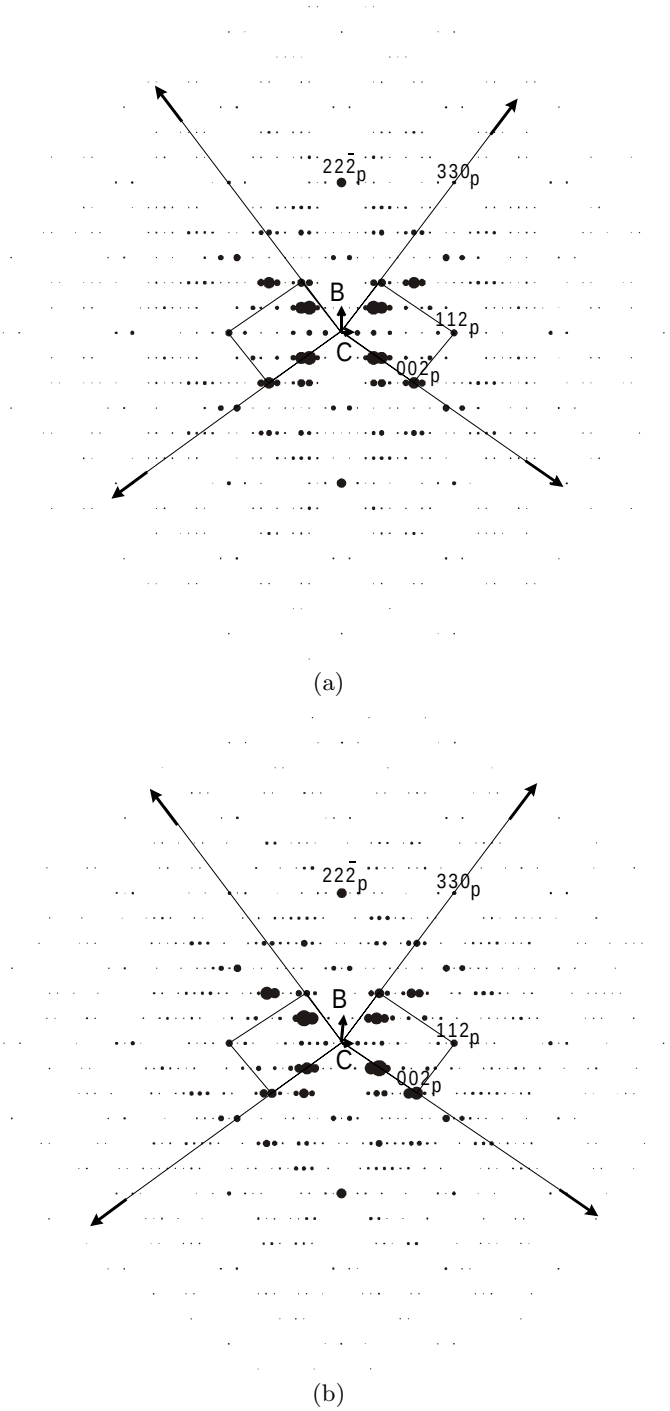

Fig. 7. Calculated [100] electron-diffraction patterns of the (a) $2m = 5+5$ and (b) $2m = 4+6$ structures. In (b) the monoclinic symmetry appears through intensity differences between the contributions of the $m = 4$ and $m = 6$ perovskite subcells.

those of the $m = 6$ part). The [010] E.D. patterns are not sensitive to the rotation-like phenomenon but they can be distinguished through the different extinction conditions of the $(h0l)$ reflections: only the $h + l = 2n$ reflections are allowed for $2m = 5 + 5$ (space group $P2_1/n$) while all the reflections are allowed for $2m = 4 + 6$ (space group $P2_1$).

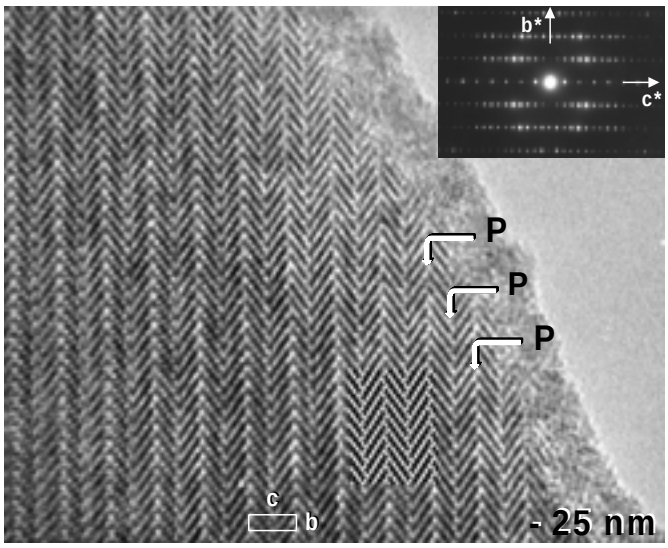

Fig. 8. Typical HREM [100] image of a $2m = 5 + 5$ crystal. The inserted image is calculated with the following parameters: high voltage 200 kV, spherical aberration constant 0.4 mm, depth of focus 10 nm, divergence semi-angle 0.85 mrad, crystal thickness 3.2 nm, focus −25 nm. The rows of pentagonal-like tunnels parallel to the **a** axis are shown by arrows. The corresponding electron diffraction pattern is shown in the right top corner.

These considerations allow the microcrystals of the batch to be quickly identified.

Thus, half of the microcrystals studied were identified as belonging to the $2m = 5 + 5$ phase, the other half corresponding either to a disordered intergrowth of different members of the family (characterized by the appearance of strong diffuse streaks parallel to the $\mathbf{c}^*$ axis) or to what could be called a semi-ordered intergrowth, *i.e.* a $2m = 5 + 5$ matrix with rather frequent intergrowth defects (characterized by diffuse streaks parallel to the $\mathbf{c}^*$ axis with nodes corresponding to the $2m = 5 + 5$ E.D. patterns; see also Fig. 9).

Another important observation is that almost no twinned microcrystals were found. Indeed, the systematic twinning phenomenon observed by the X-ray single crystal study, and which is related to the pseudo-orthorhombicity of the structure, was not observed on the microcrystals studied by electron microscopy. Considering the size of the selected area aperture in the microscope (1 μm diameter), this suggests either that the twinned domains are most often larger than a micron or that during the preparation procedure for the electron microscopy study the microcrystals were preferentially crushed in the $(\mathbf{a}, \mathbf{b})$ twin plane.

The high resolution electron-microscopy study confirms the regularity of the slab stacking. Typical contrasts of the $MPTB_p$ structure are observed along [100]. For focus value where the low electron-density zones are highlighted, the rows of perovskite type tunnels are related to white lines forming the zigzag chains. The brightest dots forming zigzag rows parallel to the **b** axis correspond to the pentagonal-like tunnels (Fig. 8). Images along [010]

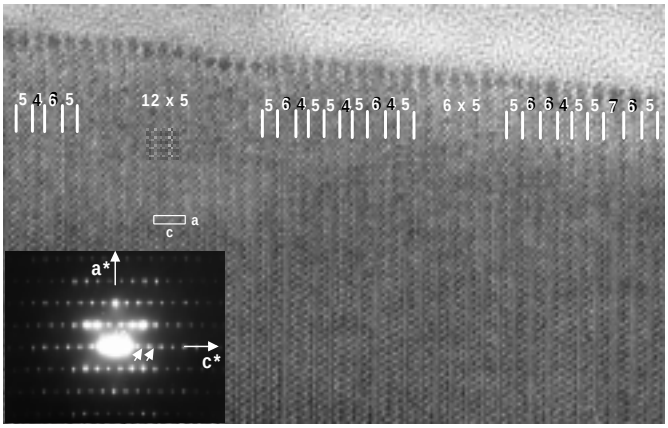

Fig. 9. Typical HREM [010] image of a so-called semi-ordered $2m = 5+5$ crystal. In the image each slab is identified through its m value. The corresponding electron diffraction pattern (left bottom corner) shows diffusion streaks parallel to the reciprocal $\mathbf{c}^*$ axis direction superimposed to the Bragg reflections of the regular $2m = 5 + 5$ pattern.

also allow the characterisation of the regularity of the slab stacking. An example of semi-ordered microcrystals is shown in Figure 9. Focus is close to 0 nm and zones of high electron-density are highlighted. Indeed, brighter dots in zigzag rows parallel to **b** are related to phosphorous atoms along the pentagonal-like tunnels, and grayer dots are related to tungsten atoms, so that it is possible to identify the member by counting them. The interesting feature is that the defective slabs are mostly of the $m = 4$ and $m = 6$ types occurring in such a way that the overall composition $m = 5$ is maintained.

3.2 Description of the crystal structure

As expected from the measured lattice parameters and the observed space group, the building principle of this new $P_4W_{10}O_{38}$ phase obeys the general construction rule of all the members of the $(PO_2)_4\,(WO_3)_{2m}$ series made of successive slabs of the WO_3-type normal to **c**, all of the same thickness.

Since m is odd, each slab is built from segments of WO_6 octahedra sharing corners of different lengths, containing alternatively 2 and 3 octahedra (Fig. 10a). In two consecutive slabs, these segments have symmetrical directions with respect to the $(\mathbf{a}, \mathbf{b})$ plane *i.e.* approximately along the [021] and $[02\overline{1}]$ directions. As seen in Figure 10b which gives an interesting projection of the slabs along **b**, a segment of two $W(2)O_6$ octahedra is bounded at each end, and at the same x level, by a PO_4 tetrahedron which links 3 of its oxygens with 3 different WO_6 octahedra of the same slab. It is only the fourth oxygen of the tetrahedron, located at the extremity of a segment of 3 WO_6 octahedra, which ensures the connection with the adjacent slab *via* a weak O–W bond.

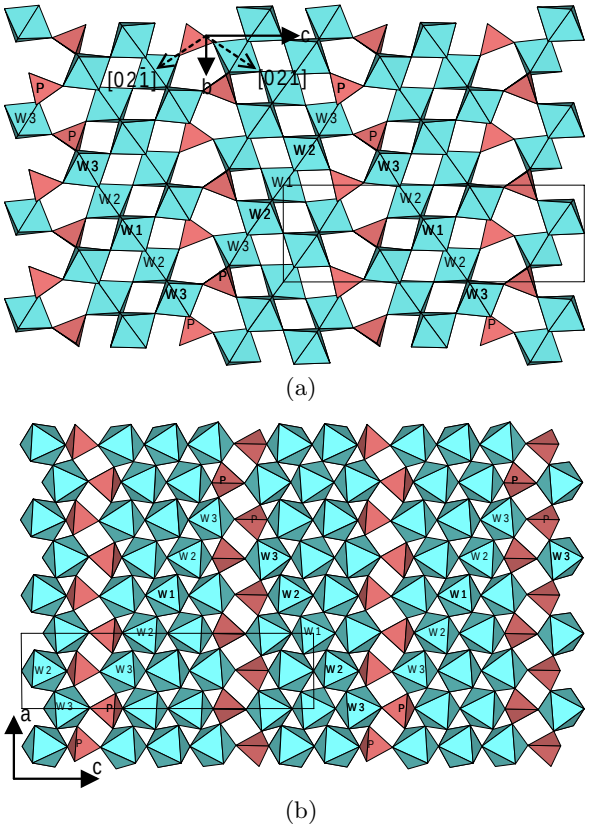

(a)

(b)

Fig. 10. Structure of the regular variety of $P_4W_{10}O_{38}$. Segments of five WO_6 octahedra delimited by two PO_4 tetrahedra are highlighted: (a) view along [100]; (b) view along [010].

3.3 Structural instabilities at low temperature

At room temperature, and below (see the X-ray pattern of Fig. 11a taken at 100 K), two sets of weak and broad diffuse lines perpendicular to the $\mathbf{a} \pm \mathbf{b}$ directions are clearly observed. Their intensities, which decrease with decreasing temperature, have nearly vanished at 25 K. In the other members of the $MPTB_p$ family, these lines are related to instabilities located on chains running along the $\mathbf{a} \pm \mathbf{b}$ directions [3,4]. These chains are built with oblique segments of m WO_6 octahedra[1]. Another kind of chain is also present in the layered structure: there are chains running along the **a** direction and composed of segments of m WO_6 octahedra tilted with respect to the chain direction. Diffuse lines associated to instabilities located on the **a** chains were observed in the $m = 4$ and $m = 6$ members. In the $2m = 5 + 5$ bronze, where the overall diffuse scattering intensity is weak, this latter kind of diffuse line was not detected. The three kinds of conducting chains give rise to three quasi-planar portions of Fermi surface. From the measurement of the relative position of the X-ray diffuse lines with respect to the Bragg reflections, one can deduce the $2k_{\mathbf{Fa}\pm\mathbf{b}}$ and $2k_{\mathbf{Fa}}$ (k_F is the Fermi wave vector) values for each quasi-1D portion of the Fermi surface.

[1] In all the regular members these chains are related by crystal symmetry.

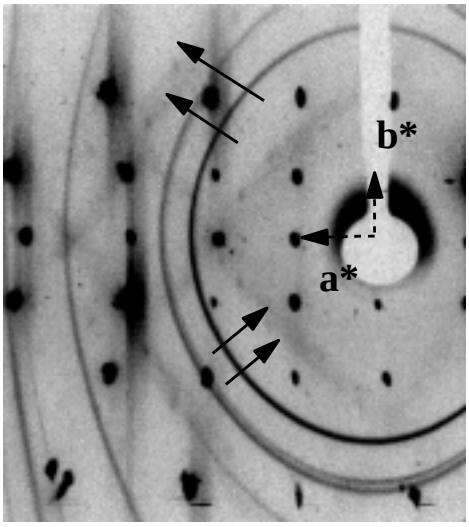

(a)

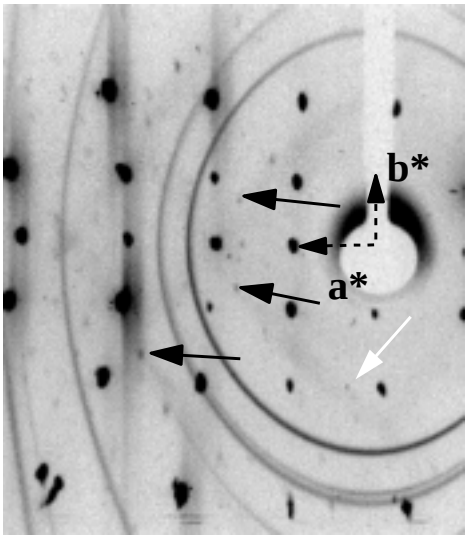

(b)

Fig. 11. X-ray pattern of the $2m = 5 + 5$ regular member taken at 100 K (a) and at 25 K (b). In (a) the diffuse lines perpendicular to the $\mathbf{a} \pm \mathbf{b}$ directions are shown by arrows. In (b) the black (white) arrows point towards the $q_{1(5)}$ ($q_{2(5)}$) satellite reflections.

The $2k_{\mathbf{Fa}\pm\mathbf{b}}$ value measured in the $2m = 5 + 5$ bronze is given in Table 4 and compared to the $2k_{\mathbf{Fa}\pm\mathbf{b}}$ and $2k_{\mathbf{Fa}}$ ones measured in the $m = 4$ and $m = 6$ members. Within the experimental errors, $2k_{\mathbf{Fa}\pm\mathbf{b}}$ for $2m = 5+5$ is the average of those found for the $m = 4$ and $m = 6$ members. This means that the Fermi surface continuously evolves from the $m = 4$ to the $m = 6$ members. The theoretical values of $2k_{\mathbf{Fa}\pm\mathbf{b}}$ and $2k_{\mathbf{Fa}}$ obtained from the extended Hückel band structure calculations by Whangbo and Canadell [4] for the $m = 4$ and 6 members are also given in Table 4. They are in relatively good agreement with the experimental results.

Below around 100 K, broad diffuse spots begin to emerge on the diffuse lines discussed above. They condense into satellite reflections below $T_{c_1} = 83$ K (± 5 K) (Fig. 11b). Another set of satellite reflections are observed below $T_{c_2} = 60$ K (± 2 K). However, the latter satellite reflections do not systematically appear at the position of the high temperature diffuse lines.

Table 4. Experimental and calculated [4] $2k_{\mathbf{Fa}\pm\mathbf{b}}$ and $2k_{\mathbf{Fa}}$ values.

member m	$2k_{\mathbf{Fa}\pm\mathbf{b}}$ experimental	$2k_{\mathbf{Fa}}$	$2k_{\mathbf{Fa}\pm\mathbf{b}}$ calculated	$2k_{\mathbf{Fa}}$
$m = 4$	0.35(2)	0.33(2)	0.295	0.41
$2m = 5 + 5$	0.38(2)	?	?	?
$m = 6$	0.39(2)	0.30(2)	0.37	0.26

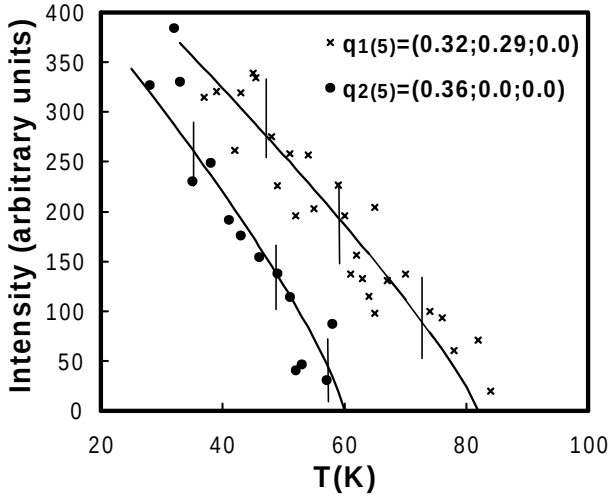

Fig. 12. Thermal dependence of the intensities of typical $q_{1(5)}$ and $q_{2(5)}$ satellite reflections.

At T_{c_1}, a structural modulation with the reduced wave vector $q_{1(5)} = \big(0.32(1), 0.29(1), 0.0(1)\big)$, using the setting of Table 1, appears. The width of the satellite reflections, which was measured along the $\mathbf{a}^*$ and $\mathbf{b}^*$ directions, corresponds to the experimental resolution. This means that at the scale of our resolution (F.W.H.M. of $\Delta q = 5 \times 10^{-2}$ Å^{-1}) long range order takes place at least in the $(\mathbf{a}, \mathbf{b})$ plane. The intensity of a typical satellite reflection is about 10^{-3} that of an average Bragg reflection, and about 10^{-5} that of the strongest Bragg reflections. The thermal variation of the intensity of a typical satellite reflection is shown in Figure 12. This quantity is related to the square of the amplitude of the structural modulation. The intensity drops continuously to zero at T_{c_1}, as already observed for the $m = 4$ and $m = 6$ members [3].

The T_{c_2} phase transition gives rise to a new set of satellite reflections at the reduced wave vector $q_{2(5)} = \big(0.36(1), 0.00(5), 0.0(1)\big)$. The resolution along the $\mathbf{a}^*$ and $\mathbf{b}^*$ directions, and the intensity of typical satellite reflections are similar to those of the first transition. The thermal dependence of the satellite intensity reported in Figure 12, shows that the intensity also vanishes continuously at T_{c_2}. In addition, no clear anomaly is observed at T_{c_2} in the thermal dependence of the $q_{1(5)}$ satellite intensity.

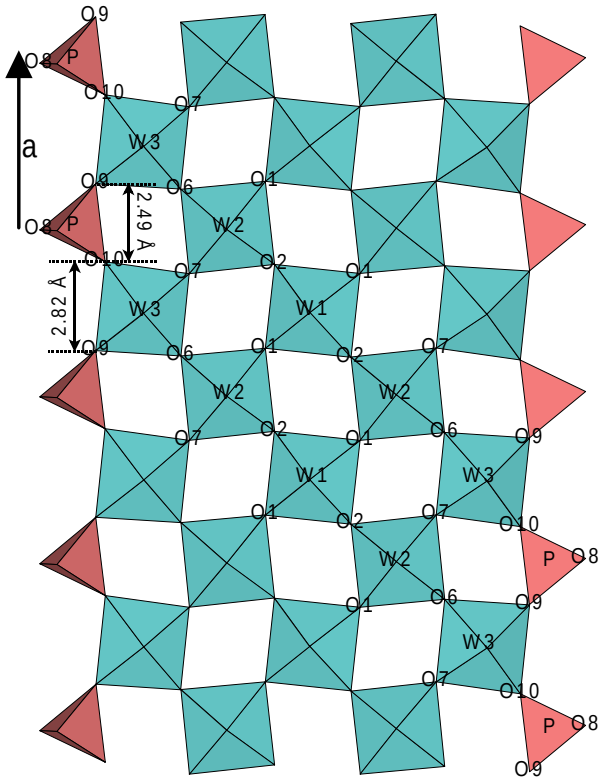

Fig. 13. Section of a slab normal to the [021] direction (defined Fig. 10a) showing the tilting of the octahedra.

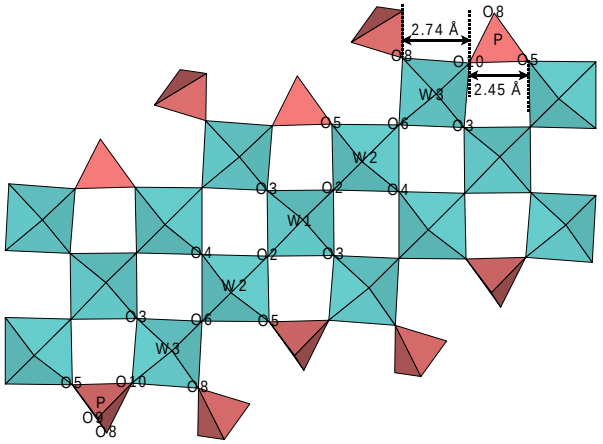

Fig. 14. Oblique section – one octahedron thick – of a WO_3-type slab in a direction perpendicular to that of Figure 13. The presence of square-shaped windows shows that there is no tilting of octahedra in this direction.

This shows that both modulations develop independently, as already observed for the $m = 4$ and $m = 6$ members.

4 Discussion

A section of slab normal to [021], corresponding to one of the W–O directions of the WO_6 octahedra, is drawn Figure 13. As for all members of the series, this section shows that all the octahedra of the slab are tilted with an angle of $\pm(6$ to $7°)$ with respect to the **a** direction. By considering the O–O interatomic distances, all the octahedra appear nearly regular, so that the empty space between the perovskite cages forms either a lozenge (Fig. 13) or a square (Fig. 14) shape. Only, the O–O distances at the border of the slabs are the exception: the O(9)–O(10) distance is thus alternately short and long (2.49 Å; 2.82 Å) (Fig. 13). This is the same for the O(5)–O(10) and O(10)–O(8) distances (2.45 Å; 2.74 Å) (Fig. 14). This illustrates the adaptability of the PO_4 tetrahedra to the WO_3-type lattice.

Inside the five WO_6 octahedra of an oblique segment (Fig. 13) bounded at each end by a PO_4 tetrahedron, the W atoms are not located at the same position. In the middle of the slab, where the $W(1)O_6$ octahedron is only surrounded by six WO_6 octahedra, the W(1) atom lies just at the centre of the octahedron, leading to six W(1)–O distances close to 1.90 Å. On each side of the slab, every $W(2)O_6$ octahedron is linked to five WO_6 octahedra and one PO_4 tetrahedron and thus the W(2) atom adopts a 2+4 oxygen coordination state with two W(2)–O distances at 1.84 Å and four distances between 1.95 Å and 2.00 Å. Finally, the $W(3)O_6$ octahedra at each end of the segment are surrounded by three octahedra and three tetrahedra and thus the W(3) atom exhibits a $3+3$ oxygen coordination with three W(3)–O bond distances of about 1.82 Å and three others distances at 2 Å (Tab. 3). This different location of W atoms in the WO_3 slabs is in agreement with those previously observed for the other members of the series. These structural data mean that W atoms exhibit certainly a formal oxidation state closer to VI ($5d^0$ configuration) at the border of the WO_3 slabs while it should be closer to V ($5d^1$ configuration) in the middle of the slabs. This implies a preferential delocalisation of the conduction electrons in the central part of the WO_6 segments. Two-dimensional electron transport properties are thus expected. The electronic dimensionality can be even reduced to one [4] owing to the anisotropy in the overlap of the conduction-electron wave functions, which leads to the formation of the previously quoted chains along the **a** and $\mathbf{a} \pm \mathbf{b}$ directions.

Resistivity, thermoelectric power, and Hall-constant measurements [15] show that $P_4W_{10}O_{38}$ ($2m = 5 + 5$) exhibits a metallic behaviour. It is however interesting to remark that the room-temperature resistivity of the $2m = 5 + 5$ regular member ($\rho \sim 5$ mΩ cm) is comparable to that of the $2m = 4 + 6$ intergrowth member, and substantially higher than that shown by the regular $m = 4$ and 6 regular members. Transport measurements, which have been performed on the same sample as that used for the X-ray diffuse scattering investigation, exhibit a metallic behaviour from room temperature to about 60 K. Around 60 K a large minimum followed by a slight bump was observed: it has been ascribed to an electronic anomaly also detected by thermopower and Hall-constant measurements. The structural transition observed here at $T_{c_2} = 60\,(\pm 2)$ K can thus be associated with

Table 5. Critical temperatures T_c and critical wave vectors q for the small m members of the $(PO_2)_4(WO_3)_{2m}$ family.

member m	T_c (K)	q
$m = 4$	$T_{c_1} = 80\,(\pm 1)$	$q_{1(4)} = (0.330(5); 0.295(5); ?)$
	$T_{c_2} = 52\,(\pm 1)$	$q_{2(4)} = (0.340(5); 0.000(5); ?)$
$2m = 5 + 5$	$T_{c_1} = 83\,(\pm 5)$	$q_{1(5)} = (0.32(1); 0.29(1); 0.0(1))$
	$T_{c_2} = 60\,(\pm 2)$	$q_{2(5)} = (0.36(1); 0.00(5); 0.0(1))$
$m = 6$	$T_{c_1} = 120\,(\pm 1)$	$q_{1(6)} = (0.385(5); 0.000(5); ?)$
	$T_{c_2} = 62\,(\pm 1)$	$q_{2(6)} = (0.310(5); 0.295(5); ?)$
	$T_{c_3} \sim 30$	$q_{3(6)} = (0.29(2); 0.11(2); ?)$

Table 6. Structure amplitudes A (arbitrary units) of characteristic reflections of the perovskite subcell.

Subcell reflection	$m = 4$	$m = 5$	$m = 6$	$m = 7$	$m = 8$	$m = 12$
$1\,1\,2_p$	0 0 12	0 0 14	0 0 16	0 0 18	0 0 20	0 0 28
	$A = 286$	$A = 320$	$A = 354$	$A = 350$	$A = 377$	$A = 421$
$1\,\bar{1}\,0_p$	2 0 0	2 0 0	2 0 0	2 0 0	2 0 0	2 0 0
	$A = 706$	$A = 724$	$A = 738$	$A = 745$	$A = 762$	$A = 787$
$1\,0\,1_p$	1 0 6	1 0 7	1 0 8	0 0 9	1 0 10	1 0 14
	$A = 585$	$A = 621$	$A = 636$	$A = 659$	$A = 664$	$A = 707$
$2\,2\,\bar{2}_p$	0 6 0	0 6 0	0 6 0	0 6 0	0 6 0	0 6 0
	$A = 421$	$A = 443$	$A = 432$	$A = 448$	$A = 433$	$A = 458$

this electronic transition. By analogy with previous findings in the $m = 4$ and $m = 6$ members of the series, it can be interpreted as probably due to the formation of a charge-density-wave (CDW). The substantial increase of magnetoresistance observed below T_{c_2} [15] indicates the presence of small carrier pockets, probably due to the incomplete CDW nesting of the Fermi surface (see below). No clear anomalies are shown by the transport properties at $T_{c_1} = 83$ K (± 5 K). Only a slight drop of the Hall constant R_H is observed below T_{c_1} [15].

It should be pointed out that, indeed, two main CDW transitions have been observed for $m = 4$ ($P_4W_8O_{32}$) and $m = 6$ ($P_4W_{12}O_{44}$) $MPTB_p$'s with the critical temperatures and wave vectors quoted in Table 5. Note that a third, but weaker transition, is observed for $m = 6$ at ≈ 30 K. In both bronzes, the stabilization of the first transition at $T_{c_1} = 80$ K ($m = 4$) and $T_{c_1} = 120$ K ($m = 6$) has been explained on the basis of a hidden Fermi surface nesting mechanism by which several quasi-1D parts of the Fermi surface are connected via a unique modulation wave vector [3,4]. The stabilization of the second CDW transition at $T_{c_2} = 52$ K ($m = 4$) and $T_{c_2} = 62$ K ($m = 6$) has been ascribed to the nesting of the electron and hole pockets remaining at the Fermi surface after the first transition.

In the $P_4W_{10}O_{38}$ ($2m = 5 + 5$) single crystal investigated here, by analogy with the $m = 4$ and $m = 6$ bronzes, the high temperature structural transition at $T_{c_1} = 83\,(\pm 5)$ K can also be explained on the basis of a similar CDW instability. The fact that this first transition cannot be detected in transport measurements could be due either to the closeness of the T_{c_1} and T_{c_2} critical temperatures or to the weakness of the gap opening after the first CDW transition (such a gap being improved after the second transition in all cases). It should be recalled that for both the $m = 4$ and $m = 6$ compounds the high temperature resistivity anomalies at $T_{c_1} = 80$ K and 120 K, respectively, are also much smaller than the low temperature ones at 50 K and 60 K [18].

The modulation wave vectors of both transitions in $P_4W_{10}O_{38}$ (Tab. 5) are very similar to those observed in the $m = 4$ ($P_4W_8O_{32}$) and $m = 6$ ($P_4W_{12}O_{44}$) members. However, for $m = 6$, the sequence of CDW transitions occurs in an opposite order to that for the $m = 4$ and $m = 5$ members. More precisely, the $(\mathbf{a}^*, \mathbf{b}^*)$ components of $q_{1(5)}$ are, within experimental errors, the average of $q_{1(4)}$ and $q_{2(6)}$. Likewise, the $(\mathbf{a}^*, \mathbf{b}^*)$ components of $q_{2(5)}$ are the average of $q_{2(4)}$ and $q_{1(6)}$. This confirms that the Fermi surface topology slightly and continuously evolves from the $m = 4$ to the $m = 6$ members. The idealized Fermi surface of the $2m = 5 + 5$ regular member deduced from the experimental values of $2k_{F\mathbf{a}\pm\mathbf{b}}$, and from the electron conservation law $2 \times 2k_{F\mathbf{a}\pm\mathbf{b}} + 2k_{F\mathbf{a}} = 1$, is represented in Figure 15. One can see that, the high temperature modulation wave vector roughly nests two quasi-1D parts of the Fermi surface out of three. As for the $m = 4$ member, the first CDW transition seems to involve one of the oblique chains along the $\mathbf{a} \pm \mathbf{b}$ directions and the chains along the $\mathbf{a}$ direction. However, while the fluctuations of chains along $\mathbf{a}$ seems to drive the high temperature CDW transition in the $m = 4$ member, only the fluctuations along the $\mathbf{a} \pm \mathbf{b}$ chains appear to be critical in $P_4W_{10}O_{38}$ ($2m = 5 + 5$). Note also that the critical wave vector of the second transition connects the third quasi-1D part of

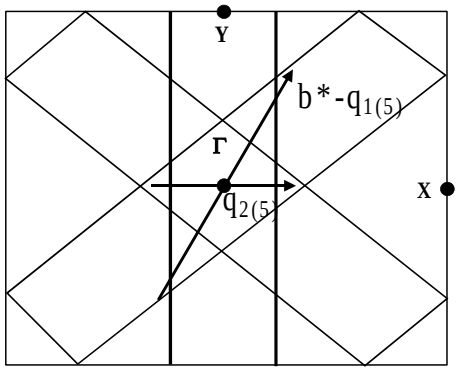

Fig. 15. Idealized Fermi surface of the $2m = 5 + 5$ regular member deduced from the experimental value of $2k_{\mathbf{Fa}\pm\mathbf{b}}$ and from the electron conservation rule $2\times 2k_{\mathbf{Fa}\pm\mathbf{b}} + 2k_{\mathbf{Fa}} = 1$ [3,4]. This rule stipulates that there are two electrons per segment of 5 octahedra (or four electrons per unit cell) shared on the three sets of **a** and $\mathbf{a}\pm\mathbf{b}$ chains defined in the text. The modulation wave vector of the successive transitions are represented.

the Fermi surface which remains unaltered after the first CDW transition.

It is also worth noting that the CDW transitions with similar critical wave vectors occur in the same order in the $m = 4$ and $m = 5$ members, with quasi-identical critical temperatures ($T_{c_1} = 80$ K and 83 K; $T_{c_2} = 52$ K and 60 K respectively). On the other hand there is a large variation of the critical temperature stabilizing the same kind of modulation between the $m = 5$ and $m = 6$ members.

5 Conclusion

A new variety of the $m = 5$ member of the monophosphate tungsten bronzes series $(PO_2)_4(WO_3)_{2m}$ has been isolated and characterized by single crystal X-ray diffraction analysis at 293 K. The structure corresponds to a regular stacking of WO_3-type slabs having the same thickness and connected through PO_4 tetrahedra according to the sequence –PO_2–$(WO_3)_5$–PO_2–$(WO_3)_5$–PO_2–. It differs from that of the so called intergrowth ($2m = 4 + 6$) variety well known for over fifteen years and corresponding to the sequence –PO_2–$(WO_3)_4$–PO_2–$(WO_3)_6$–PO_2–. The present structure perfectly integrates into the $MPTB_p$ series, being thus comparable to that of the $m = 4, 6, 7, 8$ and 12 members previously studied.

The low temperature investigation of the $2m = 5 + 5$ regular bronze confirms the previous finding for the low $m = 4$ and 6 values [3]. The $MPTB_p$ series exhibits at least two CDW instabilities. Such instabilities are associated with three kinds of chains which coexist within each WO_3-type slab because of its hidden one-dimensionality.

The results thus obtained for the regular ($2m = 5 + 5$) form of the $m = 5$ member contrasts with that exhibited by the intergrowth ($2m = 4 + 6$) compound. A recent structural investigation [19] shows that this member exhibits only a single high temperature CDW transition ($T_{c_1} = 160$ K) with a commensurate modulation wave vector $q_{1(4/6)} = (1/3, 1/3, 0)$. In addition the thermal variation of the satellite intensity is non-monotonous and presents a hysteresis phenomenon between heating and cooling cycles below T_{c_1}. The differences of structural instabilities between the two varieties of $P_4W_{10}O_{38}$ still remains to be elucidated. The presence of non equivalent CDW instabilities located in the different $m = 4$ and $m = 6$ layers should be considered to explain the special behavior of the $2m = 4 + 6$ $MPTB_p$.

References

1. *Oxide bronzes*, edited by M. Greenblatt, Int. J. Mod. Phys. B **7**, 23–24 (1993).
2. *Physics and Chemistry of low dimensional inorganic conductors*, edited by C. Schlenker, J. Dumas, M. Greenblatt, S. van Smaalen (Plenum, NATO ASI series, New York, 1996).
3. P. Foury, J.P. Pouget, Int. J. Mod. Phys. B **7**, 3973 (1993).
4. E. Canadell, M.H. Whangbo, Int. J. Mod. Phys. B **7**, 4005 (1993).
5. M.M. Whangbo, E. Canadell, P. Foury, J.P. Pouget, Science **252**, 96 (1991).
6. A. Ottolenghi, J.P. Pouget, J. Phys. I France **6**, 1059 (1996).
7. P.M. Woodward, A.W. Sleight, T. Vogt, J. Solid State Chem. **131**, 9 (1997).
8. S.L. Wang, C.C. Wang, K.H. Lii, J. Solid State Chem. **82**, 298 (1989).
9. J.P. Giroult, M. Goreaud, Ph. Labbé, B. Raveau, Acta Cryst. B **37**, 2139 (1981).
10. A. Benmoussa, Ph. Labbé, D. Groult, B. Raveau, J. Solid State Chem. **44**, 318 (1982).
11. Ph. Labbé, M. Goreaud, B. Raveau, J. Solid State Chem. **61**, 324 (1986).
12. P. Roussel, Ph. Labbé, D. Groult, B. Domengès, H. Leligny, D. Grebille, J. Solid State Chem. **122**, 281 (1996).
13. P. Roussel, G. Mather, B. Domengès, D. Groult, Ph. Labbé, Acta Cryst. B **54**, 365 (1998).
14. P. Roussel, D. Groult, A. Maignan, Ph. Labbé, Chem. Mater. **11**, 2049 (1999).
15. U. Beierlein, C. Schlenker, J. Dumas, D. Groult, Ph. Labbé, E. Balthes, E. Steep, *Proceedings of the International Conference on Synthetic Metals, Montpellier 1998*, Synth. Metals **103**, 2593 (1999).
16. V. Petricek, M. Dusek, JANA98, Institute of Physics, Praha, Czech Republic (1998).
17. A. Altomare, G. Cascarano, C. Giacovazzo, A. Guagliardi, M.C. Burla, G. Polidori, M. Camalli, J. Appl. Cryst. **27**, 435 (1994).
18. C. Hess, C. Schlenker, J. Dumas, M. Greenblatt, Z.S. Teweldemedhin, Phys. Rev. B **54**, 4581 (1996).
19. P. Foury, P. Roussel, J.P. Pouget, D. Groult, *Proceedings of the International Conference on Synthetic Metals, Montpellier 1998*, Synth. Metals **103**, 2624 (1999).